Mechanics of superelastic tensegrity braces for timber frames equipped with buckling-restrained devices

Fernando Fraternali [*], Julia de Castro Motta

Department of Civil Engineering, University of Salerno, Fisciano, SA, Italy

ABSTRACT

This work studies tensegrity bracing systems to be used as energy dissipation devices in next generation, earthquake-proof timber buildings. The examined lightweight and high-strength structures with re-centering capabilities are formed by timber members and pretensioned elements with a superelastic response, which may consist of shape memory alloy wires, cables or bars with energy dissipation capacity. In the case of bars, we assume that such members can be protected against buckling through their encasement in buckling-restrained devices, so as to respond both in tension and in compression. The work on the analyzed bracing systems presents novel results on this type of bi-directional response and the effects derived from the pretension of the superelastic elements, within an analytic formulation of the mechanical response of the structure. It includes an example dealing with a full-scale glued laminated timber frame, which compares the responses of different bracing systems in terms of the lateral force vs. drift ratio curve and ductility factor. The beneficial effects deriving from the use of buckling-restrained devices in an inverted V-braced timber frame are discussed. The presented results highlight the high potential of superelastic braces with tensegrity architecture for the design of timber frames exhibiting markedly high ductility ratios, which considerably surpass those of full-timber or timber-steel systems.

1. Introduction

The development of innovative building technologies, both in terms of construction and operation, offers a feasible solution to the urgent need to mitigate the undesired effects of global warming. A confluence of factors has pushed energy savings to the top of the global agenda: the urgent need to reduce global CO_2 emissions (United Nations Environment Programme, 2021); the climate change emergency (IPCC, 2021); the rising costs of raw materials; the soaring of energy prices; and the increasing energy consumption in developing countries (Bragagni and Xhaferraj, 2021; International Renewable Energy Agency, 2021). Data from 2021 revealed that 27% of total CO_2 emissions came from operating buildings, including heating and air conditioning, electrical systems, plumbing etc., while building construction emissions reached ~10% of the total. In an optimal scenario, green buildings can be built with biobased materials, where CO_2 is transformed into organic compounds via photosynthesis, and/or built with sustainable materials that are able to capture CO_2 during the material cycle of these products (i.e., before decaying) (Pomponi et al., 2020; Schuster and Geier, 2022).

Architects and engineers are paying increasing attention to the design of timber-based buildings, since such structures permit the integration of mass reduction, prefabrication techniques, circular economy concepts and environmental benefits in the design features (Pomponi et al.; 2020; Schuster and Geier, 2022; Salvadori, 2021; Svatoš-Ražnjević et al., 2022). The conception of earthquake-proof and wind-resistant timber buildings, especially multi-story timber buildings (MSTB), calls for the adoption of suitable energy dissipation strategies (Luo et al., 2022; Dong et al., 2020; Polastri et al., 2019; Cao et al., 2022; Sandhaas et al., 2020). MSTB can be classified into panelized, post-and-beam, modular/volumetric and hybrid systems (Salvadori, 2021; Svatoš-Ražnjević et al., 2022). Framed structures are often made of glued laminated timber (glulam), while panel systems typically use cross-laminated timber (CLT). The seismic design of MSTB can be usefully obtained, e.g., through the employment of conventional or metallic bracing systems (Luo et al., 2022; Dong et al., 2020), the post-tensioning of timber fames (Ponzo et al., 2019), and/or the coupling of a CLT core with perimeter shear-walls (Polastri et al., 2019). A correct design of the connections between the different elements of the structure is also crucial to allow

the structure to carry significantly large horizontal forces (Luo et al., 2022; Dong et al., 2020; Polastri et al., 2019; Cao et al., 2022; Sandhaas et al., 2020). It must be noted that widespread use of timber, produced to minimize CO_2 emissions, raises the issue of deforestation, and requires the adoption of suitable re-forestation policies (Pomponi et al., 2020).

The present work investigates the use of tensegrity bracing systems to create innovative structures for earthquake-resistant timber buildings. It is known that the stiffness matrix of a tensegrity structure may partially or totally (in the presence of mechanisms) derive from prestress and geometric effects, in addition to contributions arising from the mechanical properties of the components (Fraternali et al., 2015). This favors the use of biobased materials for its fabrication, as a convenient and environmentally sustainable alternative to carbon intensive materials. The bracing system investigated in this study consists of a D-shaped, lightweight and high-strength tensegrity structure (Skelton and de Oliveira, 2010), hereafter referred to as "D-brace", which exhibits recentering capabilities. It is formed by timber members and

superelastic wires, cables or bars made of a shape memory alloy (SMA).

Previous research has shown that the analyzed structure is especially able to prevent or minimize structural damage under the action of seismic forces. The design of the D-brace with a tapered profile is particularly convenient, both to architecturally conceal the structure, and to optimize its performances in terms of buckling load, displacement magnification in the transverse direction and energy (Santos et al., 2019; Fraternali and Santos, 2019; Santos et al., 2022). The present work significantly enriches these research activities, by admitting that the members of the D-brace may be able to respond both in compression and in tension, acting as bi-directional elements (Nagase and Skelton, 2014). Such a response is enabled by the encasement of the SMA elements in suitable, buckling-restrained devices (Wang and Zhu, 2018). A comprehensive, analytic modeling of the mechanical response of superelastic D-braces is presented, accounting for the application of pretension forces to the SMA elements (Sect. 2). Bi-directionality and prestress effects were not covered by the models presented in Santos
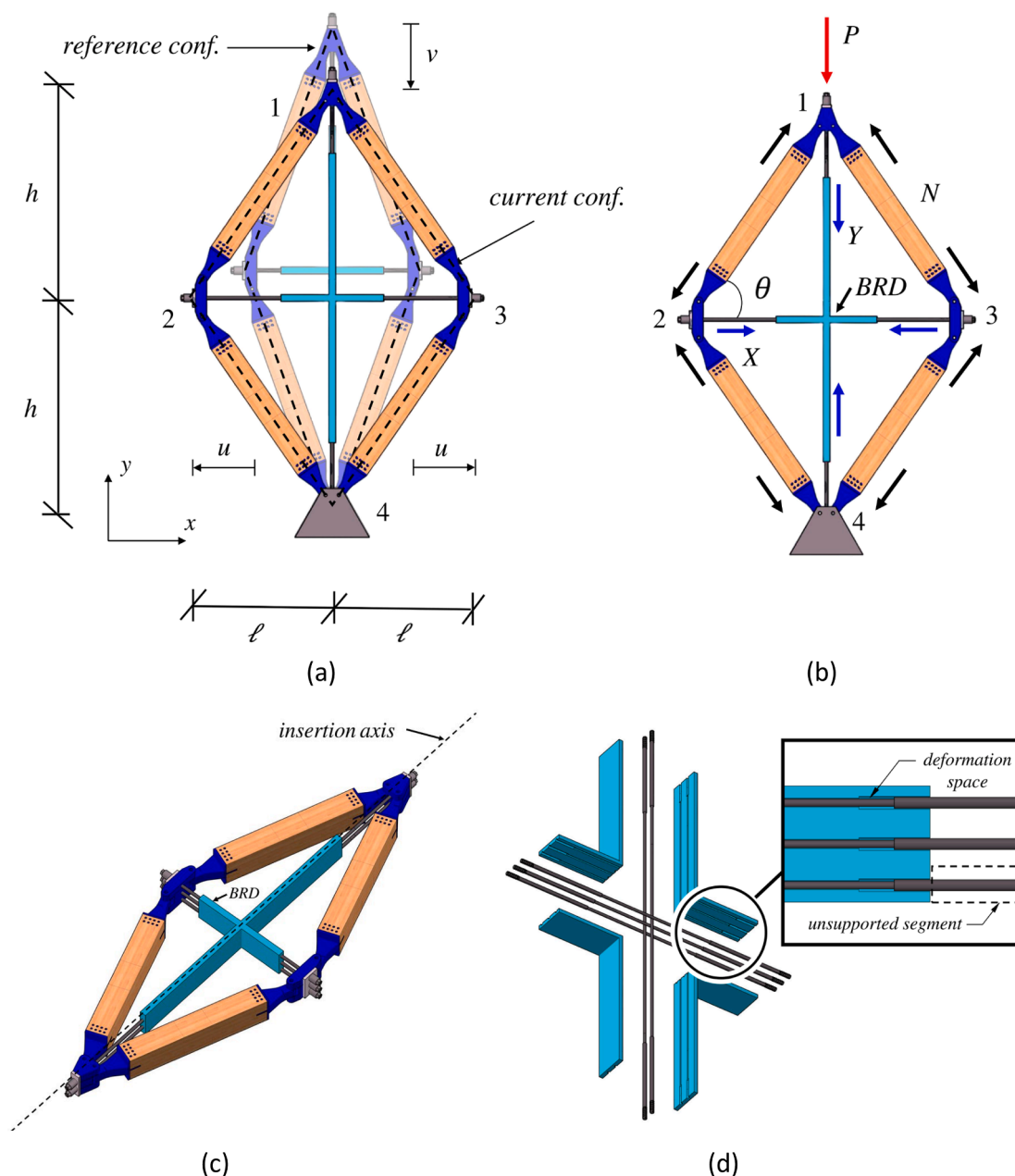

Fig. 1. Current configuration of the D-brace. (a) Displacement scheme. (b) Loading scheme. (c) 3D view of the D-brace. (d) Exploded view of the BRD.

et al. (2019); Fraternali and Santos (2019); and Santos et al. (2022), which also did not include analytic formulations of the force–displacement response nor the ductility factor of the structure. We discuss the mass-reduction and displacement amplification properties of D-braces in Sect. 3, by summarizing the results presented in Fraternali and Santos (2019) regarding such topics. Next, in Sect. 4, we present an experimental validation of the analytic constitutive equations formulated in Sect. 2, against compression laboratory tests on a physical sample. Investigations on the roles played by the geometry of the module and its insertion angle in a timber frame, with respect to the mechanical response of the structure and the ductility factor, are given in Sects. 5–7. Sect. 8 illustrates the application of a D-brace to the reinforcement of a real-example full-scale glulam frame. We compare the lateral force–displacement responses of timber frames equipped with D-braces and buckling-restrained devices, with the analogous responses exhibited by the frames studied in Dong et al. (2020). The latter are strengthened with conventional, buckling-restrained braces made of steel (BRB). The presented results highlight the enhanced ductility properties of the D-braced frames, which exhibit ductility factors markedly higher than those obtainable through more conventional bracing systems. Sect. 9 presents the design and mechanical modeling of an innovative bracing system in three-dimensions, formed by the assembly of umbrella-shaped modules. We end in Sect. 10 with concluding remarks and directions for future work.

2. Mechanical model of a prestressed D-brace

Fig. 1 illustrates the current configuration of the D-brace module under the action of a vertical force P applied to the top node 1, and in the presence of a fixed hinge at the bottom node 4 and a support condition that permits only the vertical displacement of node 1. Throughout the paper, we admit that the reference configuration of the structure under investigation is subject to a zero external force ($P = 0$) and exhibits a state of internal prestress (or self-stress), which is induced by a suitable pretension of the elements 1–4 and 2–3. The distribution of member forces depicted in Fig. 1(b) describes the structural response analyzed in previous research (see Fraternali and Santos, 2019 and references therein), in which the timber members (colored brown) act as struts that carry compressive forces, while the SMA members (colored gray) carry tensile forces.

We assume that the SMA members do not touch each other, being suitably offset in the direction perpendicular to the mid-plane of the brace. Such elements can be superelastic wires, cables or bars (Menna et al., 2015; Wang et al., 2016; Zhou et al., 2018; Li et al., 2019). In full-scale timber frames the use of SMA wires is technically not convenient, due to the remarkably high values of the lateral forces that need to be carried out (refer, e.g. to Wang et al., 2016).

The adoption of wires becomes instead useful when using D-brace modules to design smaller scale components of seismic protection devices (Menna et al., 2015), as well as to tessellate such systems in small-scale geometries over the three-dimensional space to form mechanical metamaterials (or "metabraces, cf. Fraternali and Santos, 2019). A tension-only model of the mechanical response of the SMA members can be adopted when these elements are either thin wires not able to carry significant compressive forces, or bars that are not protected against buckling. Such a model descends from a simplification of the actual response of the SMA elements under compression loading, which is expected to be characterized by the onset of large, recoverable buckling strains under small axial loads, and a remarkable reduction of the load-carrying capacity in the post-buckling regime (see, e.g., Asfaw et al. 2020). A different response is exhibited by D-bar braces showing SMA bars that are embedded in a buckling-restrained device (BRD, see Wang and Zhu, 2018), as shown in Fig. 1(d). The BRD (colored light blue in Fig. 1) is a device that encases most of the longitudinal span of the SMA bars, within grooves ending with deformation spaces that permit the stretching or contraction of the bars. The portions placed outside the

BRD have a larger diameter, as compared to the portions encased in the BRD. A gap, which can be covered with a polytetrafluoroethylene (PTFE) sheet, is left between the SMA bars and the BRD to minimize friction effects (Wang and Zhu, 2018). Such effects can be further reduced, if needed, by directly coating the SMA bars with a PTFE layer (Dunne et al., 2015).

The pretension forces acting on the SMA elements 1–4 and 2–3 are balanced by precompression forces in the timber members 1–2, 1–3, 2–4 and 4–3. Due to the symmetry of the geometry of the structure and the examined loading condition, all the timber members will carry the same axial force N, which we assume positive in compression. The SMA member 2–3 instead carries an axial force that we denote by X, while the SMA member 1–4 carries an axial force Y (both assumed to be positive in tension). The bi-directional response of the SMA elements induces an analogous response of the timber elements forming the brace, so that the distribution of forces presented in Fig. 1(b) can be inverted, with the timber members carrying tensile forces ($N < 0$) and the SMA elements carrying compressive forces ($X < 0$, $Y < 0$).

During any arbitrary transformation of the structure, which we imagine to be performed at a fixed temperature T, we suppose that the SMA elements exhibit a superelastic response (refer, e.g., to Graesser and Cozzarelli, 1991; Wang et al., 2016; Li et al., 2019), while the timber members behave as rigid bodies, due to their more massive nature. This implies that the temperature T is above the temperature A_f at which the microstructure of each SMA element is austenitic. The constitutive equations of the SMA elements are written as follows.

$$Y = f(\eta, \xi_Y), \quad X = g(\delta, \xi_X) \tag{1}$$

where η and δ respectively denote the elongation (i.e. the change of length) of the SMA members 1–4 and 2–3, measured from the rest state; ξ_Y and ξ_X are scalar (or vectorial) internal variables; and f and g are given response functions, which can be assumed rate-independent to a first approximation (Auricchio and Sacco, 1997; Auricchio et al., 2014; Menna et al., 2015). Hereafter, we agree to denote the value of the generic quantity $(\cdot)$ in correspondence to the reference configuration with the apex $(\cdot)^{(0)}$. Making use of the equilibrium equations of nodes 1 and 2 in such a configuration, we easily obtain

$$N^{(0)} = \frac{Y^{(0)}}{2\sin\left(\theta^{(0)}\right)} \tag{2}$$

$$X^{(0)} = 2\,N^{(0)}\cos\left(\theta^{(0)}\right) = \frac{Y^{(0)}}{\tan\theta^{(0)}} \tag{3}$$

where $\tan\theta^{(0)} = h^{(0)}/\ell^{(0)}$.

It is convenient to assume that the response functions f and g exhibit initial linear branches that describe the transformations of the SMA elements from the rest state to the pretensioned configuration (supposed to take place in the austenite phase), so that one can write

$$Y^{(0)} = E_Y A_Y p^{(0)} = 2k_Y p^{(0)} \bar{h} \tag{4}$$

$$X^{(0)} = E_X A_X q^{(0)} = 2k_X q^{(0)} \bar{\ell} \tag{5}$$

Here, E_Y and A_Y respectively denote the Young modulus and the cross-section area of the 1–4 element in the linear branch; E_X and A_X denote the analogous quantities relating to the 2–3 element; $p^{(0)}$ and $q^{(0)}$ indicate the axial strains associated with the pretensioning of the 1–4 and 2–3 members, respectively; $2\bar{l}$ is the rest length of 2–3; $2\bar{h}$ is the rest length of 1–4; and it results in

$$k_Y = \frac{E_Y A_Y}{2\bar{h}}, \quad k_X = \frac{E_X A_X}{2\bar{l}} \tag{6}$$

On combining Eqs. (3)–(5), we obtain

$$q^{(0)} = \frac{E_Y A_Y}{E_X A_X \tan\theta^{(0)}} p^{(0)} = \frac{E_Y A_Y \ell^{(0)}}{E_X A_X h^{(0)}} p^{(0)} \tag{7}$$

The pretensioning elongations $\eta^{(0)}$ and $\delta^{(0)}$ of the 1–4 and 2–3 elements are respectively given by

$$\eta^{(0)} = 2\left(h^{(0)} - \bar{h}\right) = 2p^{(0)}\bar{h} = \frac{p^{(0)}}{1 + p^{(0)}} 2h^{(0)} \tag{8}$$

$$\delta^{(0)} = 2\left(\ell^{(0)} - \bar{l}\right) = 2q^{(0)}\bar{l} = \frac{q^{(0)}}{1 + q^{(0)}} 2\ell^{(0)} \tag{9}$$

with $q^{(0)}$ computed through Eq. (7). It is worth remarking that the pretensioning of the brace refers to the transformation from the rest configuration (where the lengths of the SMA members are $2\bar{h}$ and $2\bar{l}$) to the reference configuration (where the lengths of the same elements are $2h^{(0)}$ and $2\ell^{(0)}$). We now move on to examine the equilibrium equations of nodes 1 and 2 in the deformed configuration (Fig. 1(b)), obtaining

$$N = \frac{X}{2\cos\theta} \tag{10}$$

$$P = 2 N\sin\theta - Y = X\tan\theta - Y = g(\delta, \xi_X)\tan\theta - f(\eta, \xi_Y) \tag{11}$$

The current values of the elongations of the SMA elements are given by

$$\eta = 2(h - \bar{h}) = \eta^{(0)} - v \tag{12}$$

$$\delta = 2(l - \bar{l}) = \delta^{(0)} + 2u \tag{13}$$

where u and v denote the displacements shown in Fig. 1(a), which are understood to be measured from the reference configuration. The hypothesis of rigid behavior of the timber members allows us to write

$$u = \sqrt{b^2 - \left(h^{(0)} - \frac{v}{2}\right)^2} - \ell^{(0)} \tag{14}$$

$$\tan\theta = \frac{h^{(0)} - \frac{v}{2}}{\sqrt{b^2 - \left(h^{(0)} - \frac{v}{2}\right)^2}} \tag{15}$$

where

$$b = \sqrt{\left(\ell^{(0)}\right)^2 + \left(h^{(0)}\right)^2} \tag{16}$$

is the constant length of such members. Eq. (11), together with Eqs. (12)–(16), defines the constitutive response P vs. v of the D-brace module. Making use of these equations, it is not difficult to recognize that such a response can be cast into the following form

$$P = g\left(\delta^{(0)} + 2\sqrt{\left(\ell^{(0)}\right)^2 + h^{(0)}v - \frac{v^2}{4}} - 2\ell^{(0)}, \xi_X\right)$$
$$\times \frac{2h^{(0)} - v}{\sqrt{4\left(\ell^{(0)}\right)^2 + (4h^{(0)} - v)v}} - f\left(\eta^{(0)} - v, \xi_Y\right) \tag{17}$$

We now examine an illustrative example of the response (17) which corresponds to a particular choice of the response functions f and g. With the aim of developing an explicit model of the force–displacement response, we consider the simple, piecewise linear constitutive response of the SMA members given in Liu et al. (2018), which does not introduce internal variables and is described by the following equation (Fig. 2)

$$Z = \begin{cases} k_1 w, & 0 \le w \le w_a, w\dot{w} \ge 0 \text{ or } w \le \beta w_a, w\dot{w} < 0 \\ (1-\alpha)k_1 w_a + \alpha k_1 w, & w_a < w \le w_b, w\dot{w} > 0 \\ (1-\alpha)k_1(w_a - w_b) + k_1 w, & w_b - (1-\beta)w_a < w \le w_b, w\dot{w} < 0 \\ (1-\alpha)k_1\beta w_a + \alpha k_1 w, & \beta w_a < w < w_b - (1-\beta)w_a, w\dot{w} < 0 \\ k_1' w, & w_a' \le w < 0, w\dot{w} \ge 0 \text{ or } w \ge \beta w_a, w\dot{w} < 0 \\ (1-\alpha')k_1' w_a' + \alpha' k_1' w, & w_b' \le w < w_a', w\dot{w} > 0 \\ (1-\alpha')k_1'\left(w_a' - w_b'\right) + k_1' w, & w_b' \le w < w_b' - (1-\beta')w_a', w\dot{w} < 0 \\ (1-\alpha)k_1\beta w_a + \alpha k_1 w, & w_b' - (1-\beta')w_a' < w < \beta' w_a', w\dot{w} < 0 \end{cases} \tag{18}$$

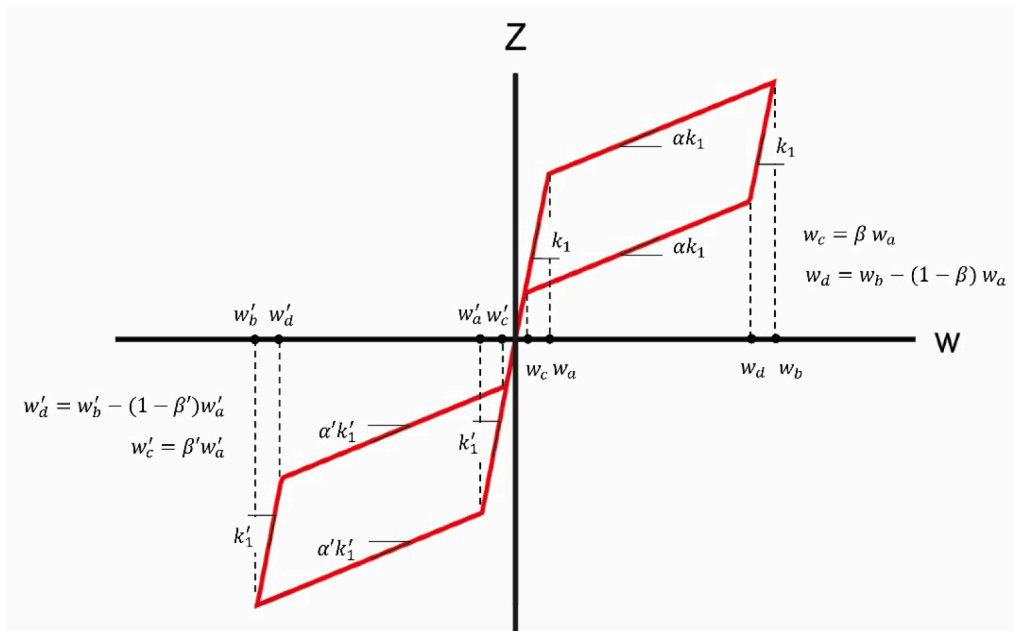In Eq. (18), the constitutive parameters affected by apexes refer to

Fig. 2. Piecewise linear response function of SMA elements reacting both in tension and in compression.

the compressive response of the SMA members, while the quantities without apexes refer to the tensile response (see Fig. 2). In the same equation, w is either η or δ; Z is either $Y = f(\eta)$ or $X = g(\delta)$; k_1 and k_1' are the slopes of the initial linear branches of the axial response; w_a and w_a' the elongations at the yield points, due to the triggering of the austenite - martensite shape transformations; w_b and w_b' are the elongations at the recoverable pseudoelastic strain limits; the scalar quantities α, α', β and β' are constitutive parameters ranging in the interval (0,1) (Fig. 2). The axial (nominal) stress σ vs. engineering strain ϵ reformulation of Eq. (18) is simply obtained by setting $\sigma = Z/A$ and $\epsilon = w/L$, with L either equal to $2\bar{h}$ (1–4 member) or to $2\bar{\ell}$ (2–3 member), A denoting the (initial) cross section area of the element. The compressive branch of the response described by Eq. (18) assumes that the buckling of such elements is prevented through the use of buckling-restrained devices (Fig. 1).

3. Mass-reduction and displacement-amplification factors

The results presented in Fraternali and Santos (2019) have shown that D-braces may exhibit remarkable performance in terms of mass-reduction and the displacement amplification ratio in the transverse direction. Let m_1 denote the mass required to the D-brace to avoid buckling under a given compression load P, and let m_0 denote the mass required to a straight, solid beam with a length of $2h - v$ to avoid the same phenomenon. On adapting Eqs. (6) and (7) of Fraternali and Santos (2019) to the notation adopted in the present work (Fig. 1), we easily obtain the following relations

$$m_1/m_0 = \left[2\left(\sin^5\left(\theta^{(0)} - \chi/2\right) \right) \right]^{-1/2} \qquad (19)$$

$$2u/v = \left(\sqrt{4\cos^2\left(\theta^{(0)}\right) - \chi\left(\chi - 4\sin\left(\theta^{(0)}\right)\right)} - 2\cos\left(\theta^{(0)}\right) \right) \Big/ \chi \qquad (20)$$

where $\chi = v/b$. In the infinitesimal displacement regime ($\chi \to 0$), it is easily found that

$$m_1/m_0 \approx \left[2\left(\sin^5\left(\theta^{(0)}\right) \right) \right]^{-1/2} \qquad (21)$$

$$2u/v \approx \tan\theta^{(0)} \qquad (22)$$

which implies $m_1/m_0 < 1$ for $\theta^{(0)} > 60.52$ deg; and $2u/v > 1$ for $\theta^{(0)} > 45$ deg. In particular, one obtains $2u/v = 1.73, 5.67, 11.43$ respectively for $\theta^{(0)} = 60, 80, 85$ deg. It has been shown in Fraternali and Santos (2019) that large displacement effects are not markedly relevant on the

m_1/m_0 ratio for $\theta^{(0)} > 60$ deg.

4. Experimental validation

We hereafter present an experimental validation of the constitutive model presented in the previous section against the experimental result conducted on a D-brace module, formed by pine wood struts with a length of 440 mm and 35 mm × 5 mm cross section, and Nickel-Titanium (NiTi) wires with 0.406 mm diameter (cross section area equal to 0.129 mm^2) and 54.5 wt% of Ni (Fig. 3(a)). The mechanical characterization of such wires was conducted at a room temperature of 20 °C, by applying seven loading-unloadying cycles with amplitude varying from 1% up to 7% of the engineering strain, at the average strain rate of 0.12%/s. These tests were conducted after having preconditioned the wires with 20 training cycles to stabilize their superelastic behavior. The force-elongation curves of the wires after preconditioning are given in Supplementary Materials.

The module under consideration features $\theta^{(0)} = 60$ deg and zero pretension of the SMA strings ($2\bar{h} = 2h_0 = 762$ mm; $2\bar{\ell} = 2\ell_0 = 440$ mm). A loading–unloading uniaxial (compression/tension) test was executed in displacement control on an electro-mechanical testing machine, by applying displacements $v = \pm 10$ mm with 0.1 mm/s displacement rate. A numerical simulation of the experimental response was carried out via Eqs. (17) and (18), assuming that the SMA wires do not react in compression, and making use of the constitutive parameters given by Eq. (23), with $L = 2\bar{h}$ in the 1–4 (vertical) string, and $L = 2\bar{\ell}$ in the 2–3 (horizontal) string. We also assumed $A_f = 10°C$, which ensures that the superelastic response of the wires can take place in test conditions.

$$\frac{k_1 L}{A} = 27 \text{ GPa}, \quad \alpha = 0.093, \quad \beta = 0.295$$

$$\frac{w_a}{L} = \epsilon_y = 0.95\%, \quad \max\left(\frac{w_b}{L}\right) = \epsilon_u = 7\% \qquad (23)$$

Fig. 3(b) shows a comparison between experimental and theoretical results for the $P - v$ curve. It is seen that the adopted mechanical model is able to reproduce the experimental response with good accuracy, both in compression ($P > 0$), and in tension ($P < 0$). The $P - v$ curve exhibits the typical, flag-shaped hysteretic aspect of the superelastic response of SMA-members (Menna et al., 2015; Wang et al., 2016; Li et al., 2019). Under compression loading, the 2–3 string is loaded in tension while the 1–4 string is slack. The $P - v$ response exhibits marked hysteresis and considerably large values of the axial load in such a loading regime, due
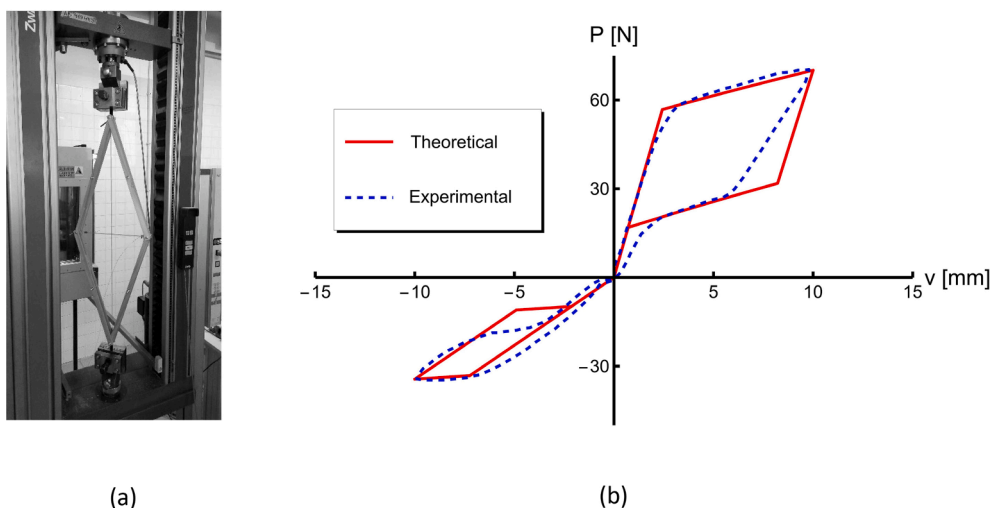

(a)

(b)

Fig. 3. Loading-unloading axial loading test on a physical sample of a D-brace featuring pine wood struts and NiTi wires. (a) Sample under testing. (b) Theoretical and experimental $P - v$ responses.

to the displacement amplification factor illustrated in the previous section. Differently, under tension loading, the $P - v$ response exhibits less marked hysteresis and lower values of P, as compared to that of the compression regime. This is due to the fact the 1–4 string is in tension and the 2–3 string is slack under such a displacement regime, and therefore no displacement amplification effects are active. The mismatch between the unloading branches of the theoretical and experimental $P - v$ curves, observed in Fig. 3(b), can be corrected through a suitable refinement of the simple constitutive model adopted in the present work. Such an extension could profit, e.g., from the assignment of different elastic moduli to the austenite and martensite phases. The current modeling, based on Eqs. (18) and (23), assumes equal elastic moduli for the two phases and ensures a good matching in terms of energy dissipated during the loading–unloading cycle (EDC). Indeed, we recorded a theoretical EDC value that differs from the experimental one by only 5%. As anticipated, we address the refinement of the constitutive model (18) to future work (see also Sect. 10).

5. Constitutive response of D-braces equipped with SMA wires

We analyze in this section the $P - v$ responses of D-brace modules equipped with NiTi wires that react only in tension, which show different geometries and the prestress levels. All the examined D-braces have height $2h_0 = 762$ mm, as in the sample studied in the previous section. We let the width $2\ell_0$ of the structure vary, in order to examine systems featuring different aspect angles $\theta^{(0)}$. The NiTi wires (or strings) are identical to those of the physical samples studied in the previous section, both in terms of diameter and constitutive parameters (see Eq. (23)). The struts are assumed to be made of a Radiata Pine glulam (GL10), which shows compression strength parallel to the grain $f_c = 26$ MPa, and modulus of elasticity $E_{GL} = 10$ GPa (Dong et al., 2020). The systems with $\theta^{(0)} = 45$ deg and $\theta^{(0)} = 60$ deg exhibit struts with a 35 mm $\times$ 5 mm cross section and are subject to the same displacement loading examined in the previous section ($v = \pm 10$ mm). The system with $\theta^{(0)} = 80$ deg instead shows struts with a 35 mm $\times$ 10 mm cross section and is subject to displacement loading with $v = \pm 1$ mm. It is easily verified that the ratio between the actual axial stiffness coefficient of the struts ($k_{GL} = E_{GL}A_{GL}/b$, A_{GL} denoting the cross section area of the struts) and the axial stiffness k_1 of the SMA tendons (when loaded in the austenitic phase) ranges from about 600 ($\theta^{(0)} = 45$ deg) down to nearly 300 ($\theta^{(0)} = 80$ deg), which justifies the assumption of a rigid response of the struts.

The $P - v$ response of a D-brace featuring $\theta^{(0)} = 45$ deg ($2\ell_0 = 2h_0 = 762$ mm) is illustrated in Fig. 4(a), for different values of the prestrains $p^{(0)} = q^{(0)}$ of the tensile elements. These quantities are expressed as fractions of the "yielding" strain ϵ_y (see Eq. (23)). The results presented in Fig. 4(a) highlight a nearly symmetric response of the structure under examination, in compression ($v > 0$) and in tension ($v < 0$), and a remarkable increase of the EDC, for increasing values of $p^{(0)}$ and $q^{(0)}$ (we observed a 67.60% EDC increase, passing from $p^{(0)} = 0$ to $p^{(0)} = 0.25\epsilon_y$). It is worth noting that a perfectly symmetric response in compression and tension is not possible, also for $\theta^{(0)} = 45$ deg and $p^{(0)} = 0$, due to the nonlinear character of Eq. (14). The maximum force in the timber struts is equal to 49.01 N (for $p^{(0)} = 0.25\epsilon_y$), and is considerably lower than buckling load $P_{buck} = 123.94$ N and the member compression strength $P_c = f_c A = 4550$ N for the analyzed material. The maximum strain in the SMA strings amounts to 1.54% (for $p^{(0)} = 0.25\epsilon_y$), and we observe that such a value is greater that the yielding strain (0.95%, cf. Eq. (23)). This explains the hysteretic nature of the responses shown in Fig. 4(a). The changes of slope observed along the loading and unloading branches, for $p^{(0)}$ and $q^{(0)}$ greater than zero, are due to the fact that both the strings 1–4 and 2–3 are reactive in the initial part of such branches, i.e., the vertical string 1–4 is engaged under compression loading ($v > 0$) and the horizontal string 2–3 is engaged under tension loading ($v < 0$).

An asymmetric response in tension and compression is instead exhibited by a D-brace module featuring $\theta^{(0)} = 60$ deg ($2\ell_0 = 440$ mm), which has the same geometry as the sample examined in Sect. 4. The $P - v$ response of the current module is graphically illustrated in Fig. 4(b) for different values of the prestrain $p^{(0)}$ of the vertical string. Such a response exhibits greater stiffness and larger maximum force P for $v > 0$ (compression loading), as compared to the response for $v < 0$ (tension loading).

It is worth noting that the prestrain of the horizontal string is equal to $q^{(0)} = 0.577p^{(0)}$ for $\theta^{(0)} = 60$ deg ($q^{(0)} = p^{(0)}/\tan\theta^{(0)}$, see Eq. (7)), and that the dissipated energy appreciably increases with increasing values of $p^{(0)}$ and $q^{(0)}$ (Fig. 4(b)). The maximum force in the timber struts is equal to 83.04 N (observe that $P_{buck} = 185.90$ N), while the maximum strain in the horizontal string is equal to 4%. The maximum axial strain of the vertical string is equal to 1.60%. We recorded a 18.85% EDC increase in the brace under examination, when passing from $p^{(0)} = 0$ to $p^{(0)} = 0.3\epsilon_y$. It is worth observing that such an increase is appreciably lower than the analogous EDC increase recorded for $\theta^{(0)} = 45$ deg. Nevertheless, referring for the sake of simplicity to the case with $p^{(0)} = 0$, one notes that the EDC of the brace with $\theta^{(0)} = 60$ deg is 65.12% larger than that of the brace featuring $\theta^{(0)} = 45$ deg.

We end the present section by examining the $P - v$ response of a narrow brace exhibiting $2\bar{\ell} = 2\ell_0 = 134$ mm and $\theta^{(0)} = 80$ deg. The results shown in Fig. 4(c) highlight that the present system exhibits austenitic-martensitic phase transformations only under compression loading ($v \in [0, 1.0]$ mm: maximum axial strain of the horizontal string equal to 4.18 %). When applying an upward displacement $v = -1$ mm, the system instead remains in the austenitic phase, as the vertical string experiences a maximum axial strain of 0.42%, which is significantly lower than the yield strain $\epsilon_y = 0.95\%$. The maximum compression force in the struts is equal to 241.64 N and it is considerably lower than the buckling load $P_{buck} = 1923.27$ N. The constitutive response depicted in Fig. 4(c) is to be expected in D-braces equipped with SMA wires that exhibit a markedly tapered profile, due to the effects of the lateral displacement amplification factor illustrated in Sect. 3. As a matter of fact, large transverse displacements are induced by small or moderately large axial displacements in such systems. It is also worth noting that a longitudinal displacement v of only 1 mm is able to produce a 4.18 % strain in the transverse string. Prestrain effects are less relevant in the present brace, as compared to the previous modules, and indeed the EDC increases only 1.59% when passing from the case with $p^{(0)} = 0$ to the case with $p^{(0)} = 0.3\epsilon_y$.

6. Constitutive response of D-braces equipped with SMA bars

We hereafter examine the $P - v$ response of a D-brace unit that is equipped with SMA rods (or bars) and exhibits the same geometry of the $\theta^{(0)} = 60$ deg module studied in the previous section. It is equipped with vertical and horizontal NiTi bars (hereafter respectively denoted Vbar and Hbar) with 3.0 mm diameter ($A = 7.069$ mm^2), encased in a BRD, so that they can respond both in tension and in compression, being subject to various levels of prestress. The pretension of the SMA bars can be applied by using, e.g., the post-tensioning systems commonly employed for commercial DYWIDAG bars (https://dywidag.com/post-tensioning). Some literature results have pointed out that SMA bars protected by buckling-restrained devices may exhibit slightly higher stiffness and strength in compression than in tension (Wang and Zhu, 2018). For the sake of simplicity, we nevertheless suppose the constitutive response of the Vbar and the Hbar to be equal in tension and compression, making use of the parameters listed in Eq. (23) in correspondence to both regimes.
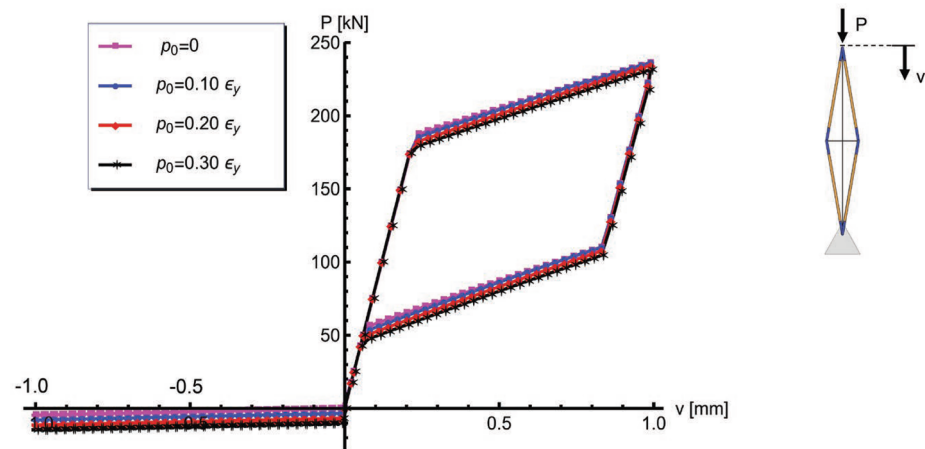
Since the SMA rods under examination exhibit a cross-section area much larger than that of the wires studied in the previous section (7.069 mm^2 vs. 0.129 mm^2), the present bracing system is expected to
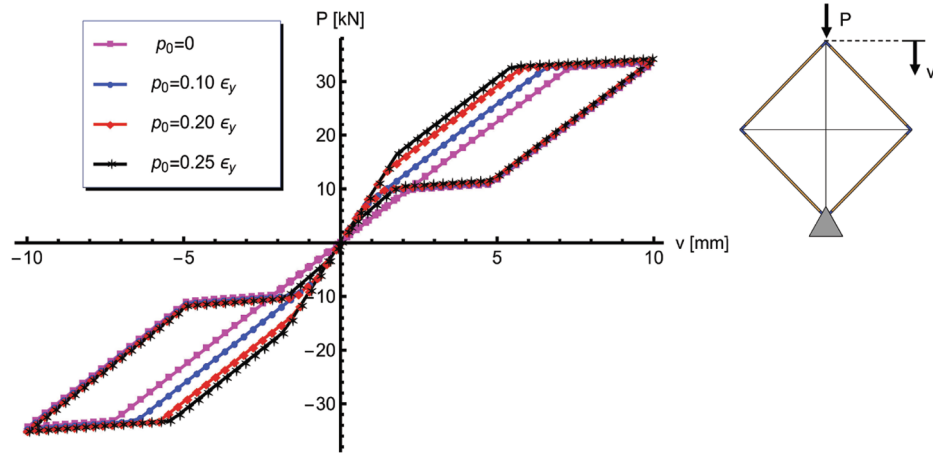
(a) $\theta^{(0)} = 45$ deg
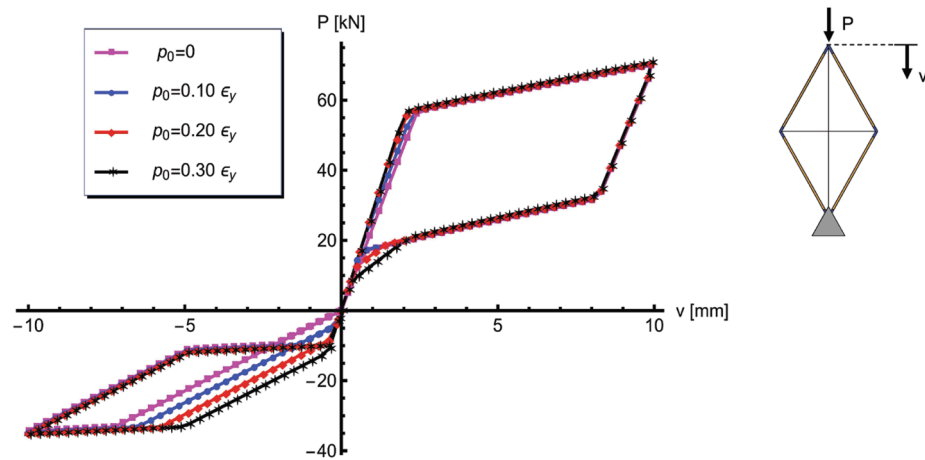
(b) $\theta^{(0)} = 60$ deg

(c) $\theta^{(0)} = 80\ deg$

Fig. 4. P-v responses of D-braces equipped with SMA wires, for different values of $\theta^{(0)}$ and the prestrain parameter $p^{(0)}$.

carry significantly higher axial forces. We therefore employ more massive timber members for its fabrication, as compared to those forming the systems analyzed in the previous section. The timber members now consist of 35 mm × 20 mm GL18 Tas Oak bars with compression strength in the direction of the grains $f_c = 50$ MPa; tension strength in the direction of the grains $f_t = 25$ MPa; and Young modulus $E_{GL} = 18.5$ GPa (https://www.lamtim.com.au/architects-glulam.html).

We examine "2-bar systems" equipped with both horizontal and vertical SMA bars (hereafter referred to as Hbar and Vbar, respectively) that are encased in a BRD, for different values of the prestrain $p^{(0)}$ applied to Vbar. In addition, we also investigate a 2-bar system without BRD (for $p^{(0)} = 0$), and a system equipped with only the Hbar encased in a BRD. The latter is not internally prestressable, since it is a statically determinate structure. The $P-v$ curves of the D-braces under consideration are shown in Fig. 5.

We initially focus our attention on 2-bar systems with BRDs, in which we observe a very light increase of the EDC (0.17%) when increasing the prestrain $p^{(0)}$ from zero up to $0.30 \epsilon_y$. This is due to the fact that the energy dissipated by the Hbar increases in compression and decreases in tension for growing values of $p^{(0)}$, while, conversely, the energy dissipated by the Vbar increases in tension and decreases in compression. Such increases and decreases of the energies dissipated by the two bars nearly cancel each other out, and therefore the overall EDC stays approximately constant.

A comparison between the response of the buckling-restrained systems equipped with one and two bars (for $p^{(0)} = 0$) reveals marked drops of the extreme values of P in compression and tension in the system equipped with only the Hbar, as compared to the 2-bar system, which is associated with a marked reduction of the EDC (the EDC of the system with only the Hbar is indeed 17.35% lower than the EDC of the system equipped with 2 bars).

We now move on to examine the $P-v$ curve of the 2-bar systems without BRDs, again considering the case with $p^{(0)} = 0$. We observe that such a curve coincides with that of the system equipped with only the buckling-restrained Hbar, under compression loading ($v > 0$). The $P-v$ curves of these two systems, however, are markedly different from each other under tensile loading ($v < 0$), and such a discrepancy leads to an

overall EDC of the system without BRDs that is 70.18% lower than that of the system showing the Hbar encased in a BRD. Overall, we can conclude that the insertion of BRDs leads to a marked enhancement of the mechanical performance of the D-brace under load reversal.

We refer the reader to Supplementary Material for the $P-v$ curves of D-braces equipped with SMA rods that show different angles $\theta^{(0)}$ ($\theta^{(0)} = 45, 80$ deg). These results demonstrate that the gaps between the responses of one-bar and two-bar systems reduce in amplitude for growing values of $\theta^{(0)}$. In the Supplementary Material we also report the strength and buckling analyses of the examined braces with SMA rods.

7. Structural ductility and maximum axial strains of the SMA elements

We now examine the insertion of D-braces in a timber frame, as shown in Fig. 6. The frame depicted in this figure exhibits two symmetrical D-braces (with respect to the vertical axis passing through the midspan), pinned connections, and acts as an inverted V-braced or chevron-braced frame (see, e.g., Yeom and Yoo, 2018, and references therein). When the frame is loaded by a rightward horizontal force F, the right brace is loaded in compression, while the left brace is loaded in tension (the opposite happens when the force F is leftward). In the special case when the braces are equipped with only transverse SMA elements and no BRD is applied, the brace being subjected to a compression force is active, while the other one does not transfer any force to the frame ($P_2 = 0$ in the case illustrated in Fig. 6). Such a configuration is not convenient from the technical point of view, since it gives rise to an unbalanced vertical load (or shear force) transferred from the braces to the beam, which in most cases produces undesired plastic collapse mechanisms in such a member (Yeom and Yoo, 2018). It is worth noting that the application of a self-stress state to a D-brace can be usefully carried out before its insertion into a frame.

Assuming rigid-body motions of the beam and the columns, the study presented in Fraternali and Santos (2019) leads us to the following relation between the horizontal displacement of the frame u_F and the transverse displacements u experienced by the engaged D-braces

$$f = 2u/u_F = [\csc(\psi)\csc(\theta) \times \left(\sqrt{\delta\sin(\psi)\cos(\psi)\sin^2(\theta)(2 - \delta\sin(\psi)\cos(\psi)) + \cos^2(\theta)} - \cos(\theta) \right)] \Big/ \delta_F \tag{24}$$
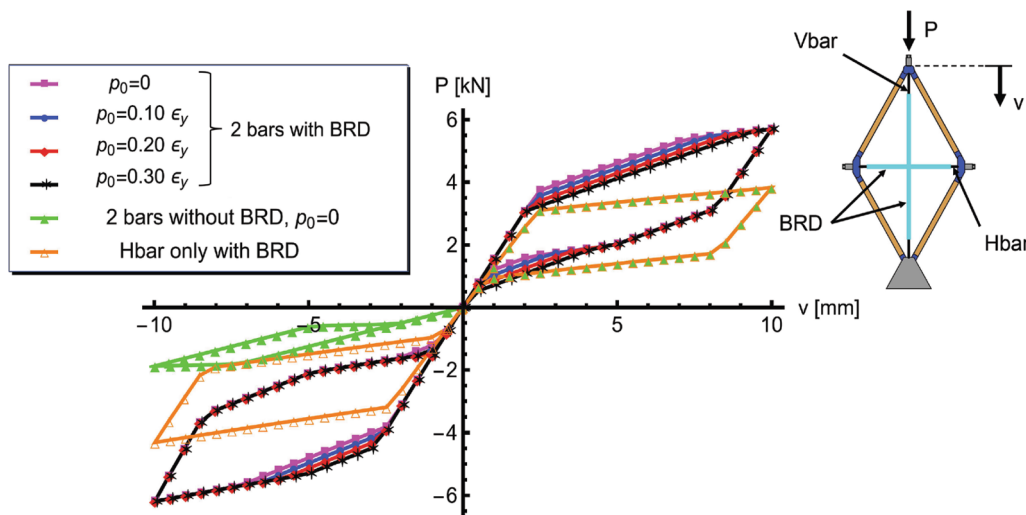

Fig. 5. P-v responses of D-braces equipped with SMA bars, for $\theta^{(0)} = 60$ deg and different values of the prestrain parameter $p^{(0)}$.
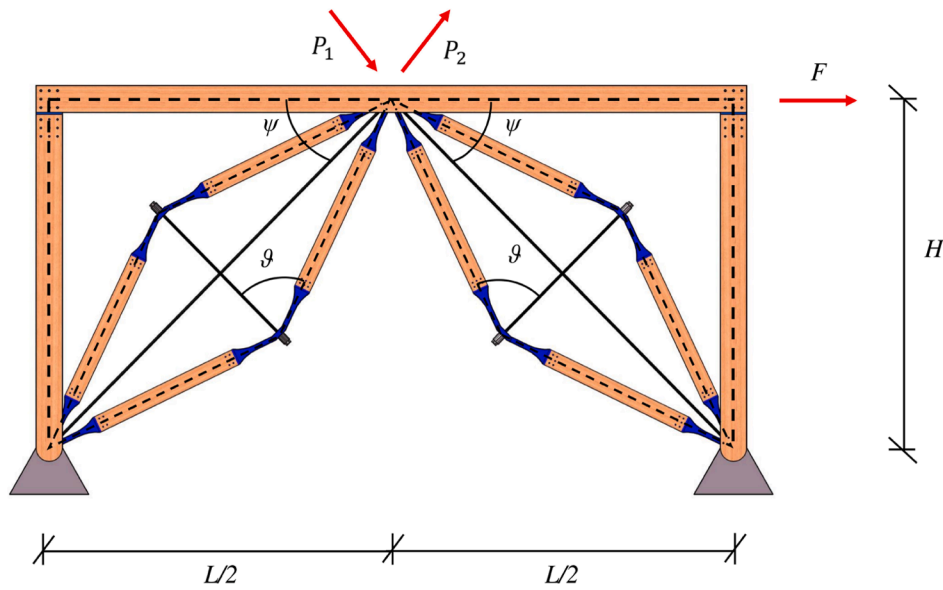
Fig. 6. Insertion of symmetrical D-braces in a timber frame.

where ψ is the insertion angle of the braces, and $\delta_F = u_F/H$ is the story drift ratio of the frame (Fraternali and Santos, 2019).

Using a capacity design approach, we now estimate the ductility factor of the braced frame as follows

$$\mu = u_{Fu}/u_{Fy} \tag{25}$$

where u_{Fy} is the lateral displacement of the frame that induces the yield displacement $u_y = 2\bar{\ell}\epsilon_y$ in the transverse tensile element of the compressed brace, and u_{Fu} is the lateral displacement that induces the maximum (ultimate) displacement $u_u = 2\bar{\ell}\epsilon_u$ in the same element, in correspondence to the recoverable pseudoelastic strain limit. Eq. (25) assumes that the SMA members forming the D-braces are the only ductile elements of the structure, while the timber members and the connections are supposed to act as not-ductile members, as a consequence of an overstrength design of such elements (Cao et al. 2022).

Making use of Eq. (24) into Eq. (25) one easily deduces that the ductility factor μ is approximated by the ϵ_u/ϵ_y ratio (assuming that the displacement amplification factor f does not significantly vary between the yield and the ultimate states). Since ϵ_y is of the order of 1% and ϵ_u can reach values in the range 5–8% for NiTi elements (Menna et al., 2015; Wang et al., 2016), such a result implies that frame structures strengthened with the braces under examination may be able to offer values of μ varying from 5 up to 8, depending on the actual values of ϵ_y and ϵ_u in the SMA elements. These values of μ are much higher than the ductility factors reported in Dong et al. (2020) for full-timber braced frames (of the order of 1.25), and for timber frames reinforced with buckling-restrained braces (of the order of 3.0–3.5).

One issue that may reduce the structural ductility is the achievement of a sufficiently large value of ϵ_u in presence of a prescribed drift ratio. Let us compute the maximum strain that the transverse SMA element of a D-brace must suffer, in order for the braced frame shown in Fig. 6 to exhibit a given value of δ_F. Using Eqs. (13) and (24) and denoting δ_u and δ_{F_u} the ultimate values of elongation of the transverse tensile element and the drift ratio, respectively, such a maximum strain demand ϵ_u is obtained as follows

$$\epsilon_u = \frac{\delta_u}{2\bar{\ell}} = \frac{\delta^{(0)} + f(\theta, \psi, \delta_{F_u})\,\delta_{F_u}H}{2\bar{\ell}} \tag{26}$$

On the other hand, making use of Eq. (9) into Eq. (26), we get

$$\epsilon_u = q^{(0)} + (1 + q^{(0)})\frac{f(\theta, \psi, \delta_{F_u})\delta_{F_u}H}{2h^{(0)}}\tan\theta^{(0)} \tag{27}$$

Restricting our analysis to the small displacement regime, we can write $f \cong \cos\psi\tan\theta$ (Fraternali and Santos, 2019), obtaining the following approximate equation for ϵ_u

$$\epsilon_u \cong q^{(0)} + (1 + q^{(0)})\sin\psi\cos\psi\tan^2\theta\delta_{F_u} \tag{28}$$

One can use Eq. (28) to select design values of the geometric variables θ and ψ, which lead to a desired ductility ratio μ. By setting $\delta_{F_u} = 1.5\%$ (maximum drift ratio of the cyclic tests on the BRB-reinforced glulam frames analyzed in Dong et al., 2020), and assuming $\epsilon_y = 1.0\%$, we were able to plot the approximated (linearized) expression of the ductility ratio $\mu \cong \epsilon_u/\epsilon_y$ as a function of θ for different values of ψ and $q^{(0)}$ (Fig. 7). It is worth observing that the predictions of ϵ_u lower than ϵ_y, obtained through Eq. (28), imply that the brace does not yield under the given value of δ_{F_u}, giving rise to ductility ratios lower than one. One can use the plots in Fig. 7 to select design values of the geometric variables θ and ψ, which lead to a desired ductility ratio μ. Fig. 7 also highlights selected ranges of values of θ and ψ that permit the achievement of μ values ranging in the interval [3,5] (design region colored light yellow) and [5,7] (design region colored light orange). It must be noted that the attainment of such large ductility ratio values
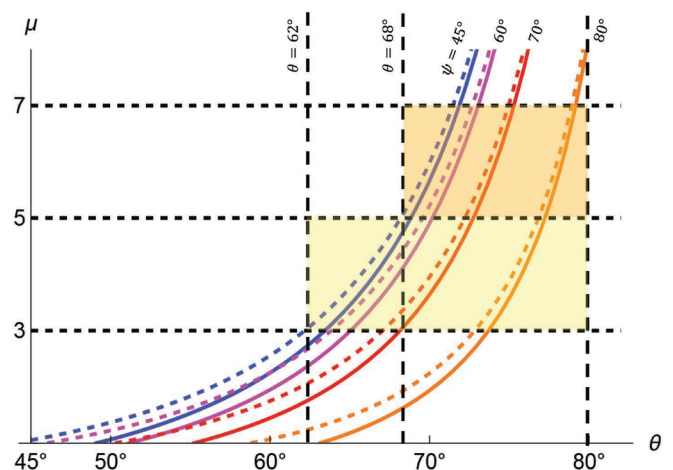

Fig. 7. Plots of μ vs. θ for different values of ψ (assuming $\epsilon_y = 1.0\%$ and $\delta_{F_u} = 1.5\%$). The solid curves refer to the case with $q^{(0)} = 0$ while the dashed curves refer to the case with $q^{(0)} = 0.3\epsilon_y$.

calls for the adoption of sufficiently tapered braces ($\theta > 62$ deg), and that the minimum needed value of θ grows with increasing values of the insertion angle ψ.

8. D-brace reinforcement of a full-scale glulam frame

We now move on to analyze the reinforcement of the full-scale glulam frame studied in Dong et al. (2020) with D-braces. Such a frame is composed of a 315 mm × 585 mm GL10 beam and 315 mm × 315 mm posts made of the same material. The frame elements are connected to each other through either doweled or screwed connections. Fig. 8(a) illustrates the layout of the D-brace reinforcement of the frame under consideration, which shows hinge connections between the different members, and D-braces aligned with the BRBs studied in Dong et al. (2020) ($\psi = 42$ deg). The out-of-plane buckling of the frame is prevented, thanks to the presence of transverse restraints. The D-braces are assumed to be equipped with 315 mm × 250 mm GL18 Tas Oak members featuring the mechanical properties reported in Sect. 6 and only transverse SMA rods. We employ rows of 3 parallel Ti-Ni bars featuring 20 mm diameter, which are encased in BRDs and are able to react both in tension and in compression ("D-braced frame"). The mechanical properties of the NiTi bars studied in Wang et al. (2016) are adopted in the present example. These bars were subjected to a pre-heating furnace treatment at 400 °C for 45 min and then water cooled to minimize residual strain effects. Residual strain effects are indeed to be expected in untreated SMA bars, and there is some experimental evidence to suggest

that they become more relevant in large size bars (Li et al., 2019). The adoption of the following constitutive parameters

$$\frac{k_1 L}{A} = \frac{k_1' L}{A} = 30 \text{ GPa}, \quad \alpha = \alpha' = 0.033, \quad \beta = \beta' = 0.333 \tag{29}$$

led us to suitably average the dissipative features of the stress–strain curves presented in Fig. 3 of Wang et al. (2016) for pre-heated SMA bars, upon neglecting residual strain effects, which are beyond the scope of the present study. In line with the experimental results presented in Wang et al. (2016), we assume that the superelastic austenite–martensite phase transformation of the SMA bars can take place at room temperature. We employ the BRD graphically illustrated in Fig. 8 (c), which is made of a carbon-fiber reinforced polymer (CFRP) with longitudinal Young modulus of 441 GPa and density of 1870 kg/m3 (Liu et al. 2015). The use of such a material, in place of steel (which was instead adopted in Wang and Zhu, 2018), is motivated by the need to reduce the deflection of the SMA bars due to the self-weight of the BRD.

The linearized analysis presented in the previous section leads us to estimate a ductility ratio $\mu = 5.63$ for the D-braced frame, which is markedly larger than the ductility ratios observed the BRD frames studied in Dong et al. (2020).

A simulation of the lateral force F vs. displacement drift ratio δ_F curve of such a frame model was carried out supposing a fully rigid response of the timber elements forming the braces and the frame. Based on such assumptions, we derive the force–displacement response of the D-braced frame in analytic form, in finite kinematics, making use of the
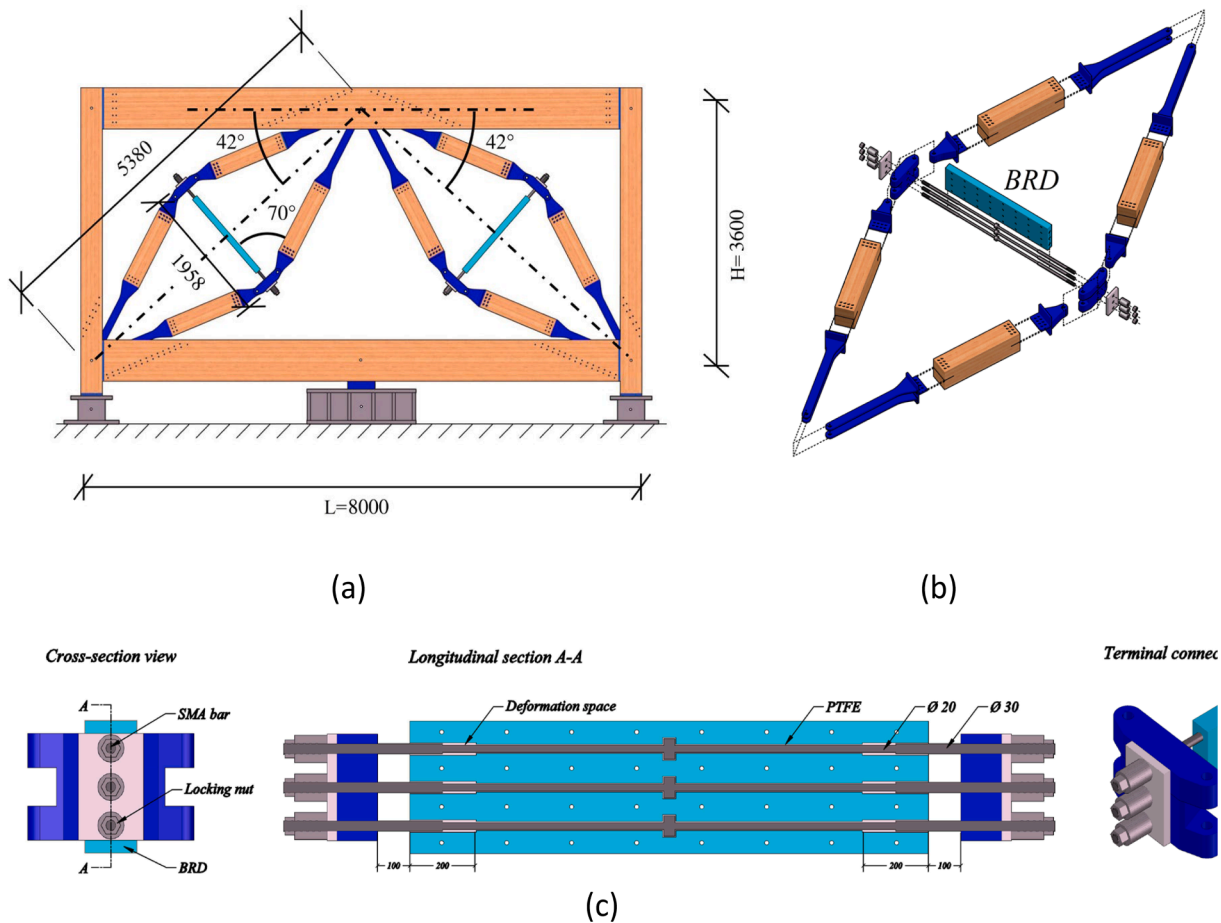

(a)

(b)

(c)

Fig. 8. Illustration of the D-braced frame. (a) Schematic layout of the reinforcement of the glulam frame studied in Dong et al. (2020) with two symmetrical D-braces (dimensions in mm). (b) D-bar brace equipped with SMA bars encased in a BRD. (c) Layout of the buckling-restrained device with dimensions 1347 × 356 × 79 mm considered in the present study.

following equations

$$F = P_1 \cos\psi_1 - P_2 \cos\psi_2$$

$$v_1 = \sqrt{\left(2h^{(0)}\cos(\psi_1) - L/2 + u_F\right)^2 + \left(2h^{(0)}\sin(\psi_1) - H\right)^2}$$

$$v_2 = -\sqrt{\left(-2h^{(0)}\cos(\psi_2) + L/2 + u_F\right)^2 + \left(-2h^{(0)}\sin(\psi_2) + H\right)^2} \qquad (30)$$

that assume u_F directed rightward, as in Fig. 6. Here, P_1 and P_2 are the axial forces carried by the two braces (positive in compression); v_1 and v_2 are their elastic displacements along the longitudinal axes; $\psi_1 = \tan^{-1}(H/(L/2-u_F))$ and $\psi_2 = \tan^{-1}(H/(L/2+u_F))$ are the insertion angles of the braces in correspondence to the deformed configuration of the frame. Similar relationships are easily found for u_F directed leftward. We now set $u_F = \delta_F H$ and let δ_F vary between -1.5% and $+1.5\%$ through incremental steps $\delta_F = 0.0015\%$. Using the P_1 vs. v_1 and P_2 vs. v_2 relations of the braces, derived from Eqs. (17) and (18), into Eq. (30), we are able to predict the F vs. u_F response of the frame. Such a response is compared in Fig. 9 with those of the BRB frames studied in Dong et al. (2020), in presence of inserted steel plates with doweled connections (S-D BRB frame), and side steel plates with screwed connections (S-S BRB frame; see Supplementary Material for additional details on these frames). The simulated response of the D-braced frame leads us to estimate a ductility ratio $\mu = 5.65$, which just slightly differs from that computed on the basis of the simplified analysis presented in the previous section (0.34% mismatch).

The comparisons shown in Fig. 9 reveals that the D-braced frame develops a considerably larger maximum horizontal force ($F_{max} = 1342.2$ kN), over the BRB reinforced frames ($F_{max} = 746.7$ kN and 748,1 for the S-D and the S-S frames, respectively in in Dong et al., 2020). It should also be noted that the D-braced frame exhibits slightly lower energy dissipation per cycle, which is approximately 7% and 11% lower than the EDC exhibited by the frames reinforced with S-D and S-S BRBs, respectively. Such a property can be effectively modulated by playing with the size and material of the SMA elements in the D-braces. It must also be considered that the D-braces exhibit a perfect re-centering response, in the absence of residual strain effects.

The achievement of a considerably large value of F_{max} obviously calls for an accurate overstrength design of the frame elements and the connections, which is outside the area of focus of the present study. A detailed structural analysis of the BRD shown in Fig. 8(c) is also left for future work. Such a study will examine different material choices, including steel, and a variety of composite materials alternative to CFRP, such as, e.g., glass-fiber composites. We refer the reader to Supplementary Material for the strength analysis of the D-braces.

9. Three-dimensional D-bar braces

The present section examines the three-dimensional version of the D-bar bracing system shown in Fig. 10, which is inspired by the sloped columns designed by SARC Architects for the Finnish Forest Research Centre located in Joensuu, Finland, also known as "Metla Building" (Archdaily, 2009).

The system shown in Fig. 10 is composed of umbrella-shaped assemblies of the bipyramid 3D brace units proposed by Skelton and de Oliveira, 2010, which we assume to be equipped with BRDs. These systems can be interposed between two floor slabs of a timber building (see, e.g., the foyer structure of the Metla Building illustrated in Archdaily, 2009), and aim to carry both horizontal and vertical forces. The basic module of the system under consideration is composed of four 3D D-bars and is contained within a $L \times L \times H$ box in the reference configuration, H denoting the height and L denoting the side length of the box (Fig. 11). We refer the geometry of the 3D module to a x, y, z Cartesian frame that shows the x and y axes aligned with the diagonals of the enclosure box, letting $\psi^{(0)} = \tan^{-1}(H/(L\sqrt{2}/2))$ denote the insertion angle of all the braces in the reference configuration (Fig. 11(a)).

Let us assume that the axial force (P) vs. axial displacement (v) response of the 3D D-bar unit has been determined, making use of an analytic approach similar to that presented in Sect. 2 of this paper, or a numerical approach (see, e.g., Sect. 4 of Santos et al., 2022). We wish to determine the constitutive response of the three-dimensional brace module shown in Fig. 11(a), under the action of a vertical load with amplitude Q and horizontal forces with amplitudes F_x and F_y, making use of an approach that suitably generalizes the one presented in the previous section. Assuming a rigid response of the floor slabs to in-plane and out-of-plane forces, we let P_1, P_2, P_3 and P_4 denote the axial forces carried by the 3D brace units forming the module under examination. The force diagrams shown in Fig. 11(a) assume that such forces are compressive, which is the case when Q is sufficiently larger than F_x and F_y.

We now let $P_1^{(Q)}$, $P_2^{(Q)}$, $P_3^{(Q)}$ and $P_4^{(Q)}$ denote the portions of the axial forces carried by the braces, which are produced by the action of the sole vertical load Q. By enforcing the equilibrium equations of the nodes we obtain
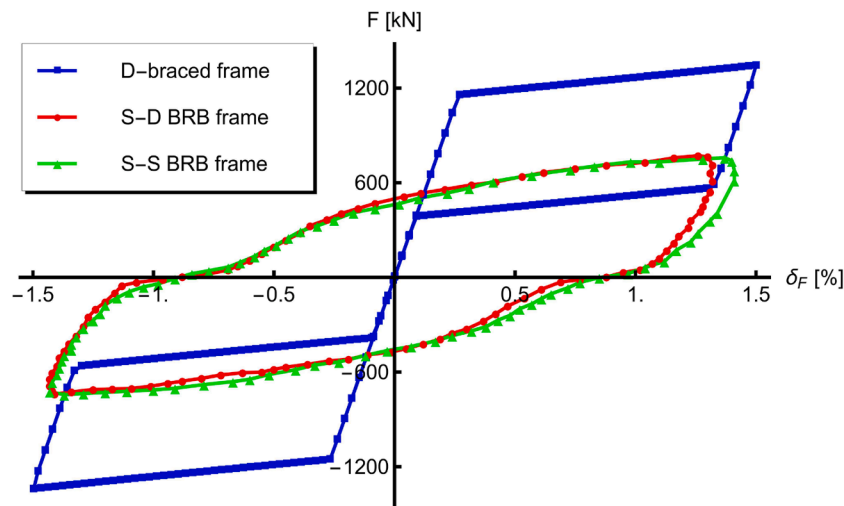

Fig. 9. Comparison of force-drift ratio responses for the D-brace reinforced glulam frame and the BRB-reinforced frames analyzed in Dong et al. (2020).
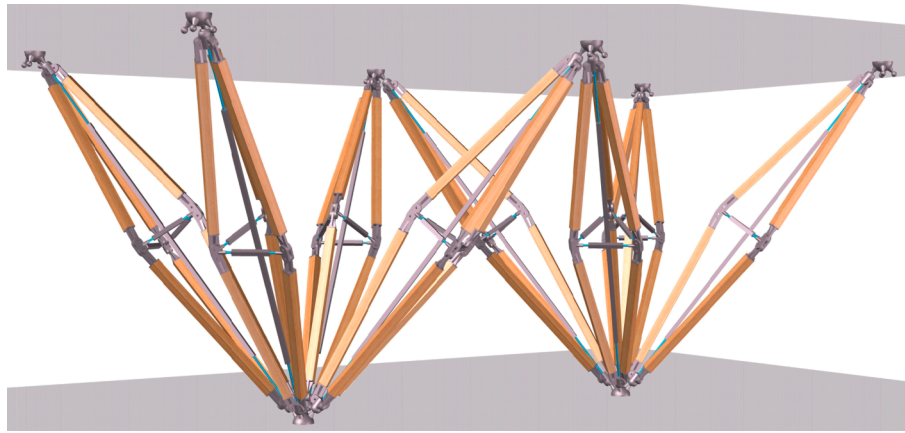
Fig. 10. Three-dimensional D-brace modules inspired by the sloped columns designed by SARC Architects for the Metla Building in Joensuu, Finland (Arch-daily, 2009).
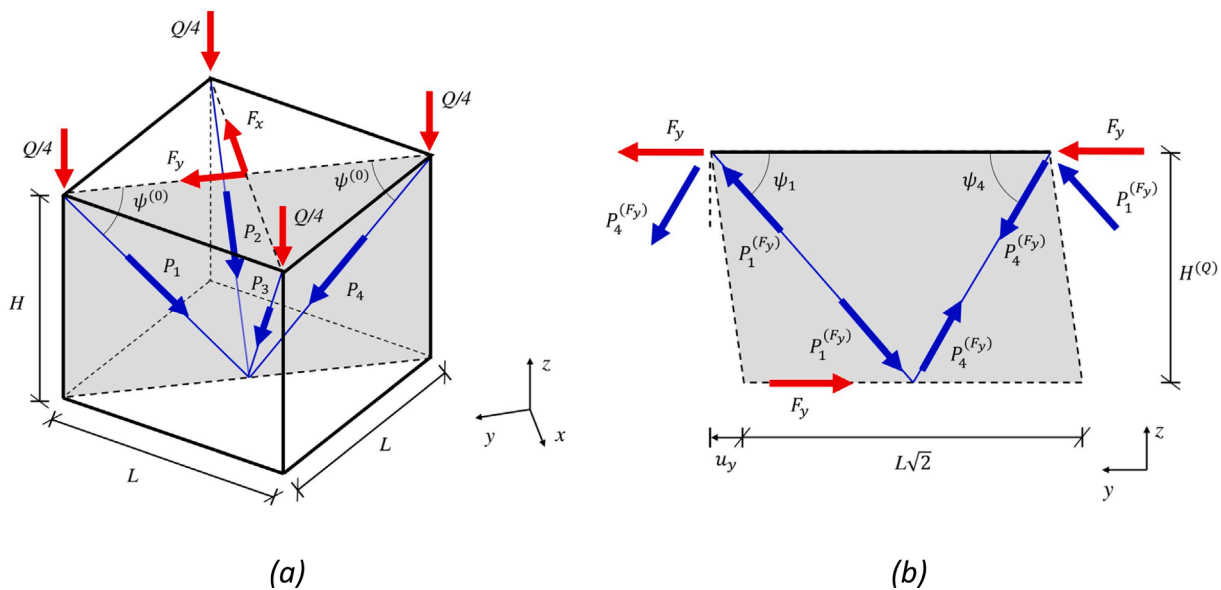

(a)   *(b)*

Fig. 11. (a) Box enclosing the basic module of the 3D bracing system shown in Fig. 10, with indication of the axis lines of the braces (dashed blue lines) and the active forces. (b) Force diagram over a diagonal section loaded by the horizontal force F_y, which reports also the interactions with the adjacent modules.

$$P_1^{(Q)} = P_2^{(Q)} = P_3^{(Q)} = P_4^{(Q)} = \frac{Q}{4\sin(\psi^{(Q)})} \qquad (31)$$

where $\psi^{(Q)} = \tan^{-1}((H - u_z)/(L\sqrt{2}/2))$ denotes the angle formed by all the braces with the horizontal plane (or insertion angle) in correspondence to the equilibrium configuration under the action of Q, which we will hereafter refer to as Q-configuration. Due to the assumption of a rigid response of the floor slab, it is easily recognized that the deformation taking the module from the reference configuration (under zero external forces) to the Q-configuration is characterized by equal vertical displacements of the top nodes. We let u_z denote the amplitude of such displacements, assumed positive downward. It is not difficult to verify that the elastic displacement exhibited by all the braces in the Q-configuration along their longitudinal axes is given by

$$v^{(Q)} = \sqrt{\left(2h^{(0)}\sin(\psi^{(Q)}) - H + u_z\right)^2 + \left(2h^{(0)}\cos(\psi^{(Q)}) - L\sqrt{2}/2\right)^2} \qquad (32)$$

where $2h^{(0)}$ denotes the axial length of all the braces in the reference configuration. Using Eqs. (31) and (32) and the $P-v$ laws of the braces one can numerically compute u_z, thus obtaining the constitutive

equation of the module under vertical loads.

Let us assume that the floor slab is supported by a grid of beams connected to the braces and directed along the $x-$ and $y-$axes shown in Fig. 11(a). Upon neglecting second order effects due to out-plane displacement of the braces forming the 3D module, we can assume that the action of the force F_y on the Q-configuration gives rise to elastic axial forces $P_1^{(F_y)}$ and $P_4^{(F_y)}$ in the braces #1 and #4 and induces a uniform displacement u_y of the top nodes of the module along the y-axis. Similarly, the action of F_x gives rise to elastic axial forces $P_2^{(F_x)}$ and $P_3^{(F_x)}$ in the braces #2 and #3 and a uniform displacement u_x of the same nodes. Fig. 11(b) shows the force diagram produced by the action of F_y on a diagonal section of the module that intersects the braces #1 and #4.

It is not difficult to recognize that the displacement u_y produces the following elastic axial displacements of the braces depicted in Fig. 11(b)

$$v_1^{(F_y)} = -\sqrt{\left(-2h^{(Q)}\cos(\psi_1) + L\sqrt{2}/2 + u_y\right)^2 + \left(-2h^{(Q)}\sin(\psi_1) + H^{(Q)}\right)^2}$$

$$v_4^{(F_y)} = \sqrt{\left(2h^{(Q)}\cos(\psi_4) - L\sqrt{2}\big/2 + u_y\right)^2 + \left(2h^{(Q)}\sin(\psi_4) - H^{(Q)}\right)^2} \tag{33}$$

where $2h^{(Q)}$ denotes the axial length of all the braces in the Q-configuration, and we have set $H^{(Q)} = H - u_z$; $\psi_1 = \tan^{-1}(H^{(Q)}/(L\sqrt{2}/2 + u_y))$; $\psi_4 = \tan^{-1}(H^{(Q)}/(L\sqrt{2}/2 - u_y))$. The equilibrium equation of the nodes forming the section shown in Fig. 11(b) along the y-axis gives

$$F_y = P_4^{(F_y)}cos(\psi_4) - P_1^{(F_y)}cos(\psi_1) \tag{34}$$

Proceeding in a similar fashion, one can obtain equations relating F_x with the corresponding axial forces and axial displacements of the braces #2 and #3. Such equations, once combined with the $P-v$ laws of the braces, lead us to finally derive the constitutive laws of the module, which relate F_x and F_y to u_x and u_y.

10. Concluding remarks

We have presented mathematical models of the mechanical response of tensegrity braces equipped with superelastic tensile elements, to be used for the strengthening of earthquake-proof and wind resistant timber buildings. The proposed models describe the mechanical response of the examined bracing systems and their ductility properties, by generalizing the results presented in previous studies (Santos et al., 2019; Fraternali and Santos, 2019; Santos et al., 2022), in order to account for the presence of buckling restraining devices that permit a bidirectional (tension/compression) response of the SMA members. The latter in turn induces an analogous response of the timber elements forming the brace. This type of response, which was not analyzed in the previously published literature on the subject, leads to significant improvements of the structural response in terms of energy dissipation capacity. We have developed an analytic modeling of the force–displacement response of the analyzed structures including prestress effects, which were also not covered by the study presented in Fraternali and Santos (2019). We have also presented a three-dimensional bracing system composed of 3D D-bar units, which are joined to form novel, umbrella-shaped modules. An analytic procedure has been formulated to determine the constitutive equations of such a system under the action of vertical and horizontal forces.

The assumptions made about the rigid response of the timber members allows us to apply the analytic results presented in this study to braces that employ members exhibiting axial stiffness significantly larger than that of the SMA elements. The use of timber members, however, merits special attention, since its use engenders significant environmental benefits. The latter mainly derive from the possibility to realize lightweight structures that contribute to reducing the carbon footprint of the building; can be assembled using convenient prefabrication techniques; and are suitable for reuse (Schuster and Geier, 2022). We have shown that the studied bracing systems can be employed to design timber frames featuring ductility factors markedly higher than those available for more conventional, full-timber or hybrid bracing systems (Dong et al., 2020), as a consequence of an optimized design of the geometry of the brace and thanks to its noticeable displacement amplification property in the transverse direction. Their adoption to form inverted V-braced fames proved to greatly benefit from the use of BRDs. These devices indeed permit the dissipation of considerably large energies per cycle during lateral-force loading, even in the presence of the narrow (tapered) profiles of the braces. It has also been shown that the timber members of the analyzed frames are able to avoid compression and tension yielding, as well as buckling, under the prescribed loading conditions, and that the energy dissipation properties of the D-braces can be appreciably amplified by suitably prestraining the tensile members, when using braces equipped with tension-only SMA wires.

We address an extensive experimental study about the response of D-braced timber frames, both full-scale and reduced-scale, to future work.

Additional lines of future research will be focused on the refinement of the mechanical model presented in this work, accounting for different elastic moduli of the austenite and martensite phases; thermomechanical-, residual-strain-, and strain-rate-dependent effects in the SMA elements (Brinson, 1993; Chang et al., 2006; Ozbulut and Hurlebaus, 2010; Li et al., 2019; Wang et al., 2022); as well as the modeling of damage/plasticity effects in the timber members (Cao et al., 2022). We also intend to investigate on the use of various tensile members with energy dissipation capacity in such systems, as an alternative to SMA elements, such as, e.g., thermoplastic polyurethane (TPU) cables and membranes (Fraternali et al., 2021; de Castro Motta et al., 2022). Additional future work will be aimed at extending the three-dimensional design presented in Section 9 to modules with different geometries, making use, e.g., of a suitable generalization of available results on pantographic metamaterials (dell'Isola et al., 2019). Finally, we intend to develop future research to investigate the optimal seismic design of MSTB equipped with D-braced frames, making use of artificial intelligence techniques (Hmede et al., 2022; Hu et al., 2022).

Declaration of Competing Interest

The authors declare that they have no known competing financial interests or personal relationships that could have appeared to influence the work reported in this paper.

Data availability

The Mathematica® code employed for the prediction of the mechanical response of the timber frame analyzed in Sect. 8 can be provided by the corresponding author upon request.

Appendix A. Supplementary material

Supplementary material to this article can be found online at https://doi.org/10.1016/j.ijsolstr.2023.112414.

References

ArchDaily, METLA Forest Research Centre/SARC Architects 0719-8884 2009 Accessed 4 June 2023. https://www.archdaily.com/15951/metla-forest-research-centre-sarc-architects. ISSN.

Asfaw, A.M., Sherif, M.M., Xing, G., Ozbulut, O.E., 2020. Experimental investigation on buckling and post-buckling behavior of superelastic shape memory alloy bars. J. Mater. Eng. Perform. 29 (5), 3127–3140. https://doi.org/10.1007/s11665-020-04815-9.

Auricchio, F., Bonetti, E., Scalet, G., Ubertini, F., 2014. Theoretical and numerical modeling of shape memory alloys accounting for multiple phase transformations and martensite reorientation. Int. J. Plasticity 59, 30–54. https://doi.org/10.1016/j.ijplas.2014.03.008.

Auricchio, F., Sacco, E., 1997. A one-dimensional model for superelastic shape-memory alloys with different elastic properties between austenite and martensite. Int. J. Non-Linear Mech. 32 (6), 1101–1114. https://doi.org/10.1016/S0020-7462(96)00130-8.

Bragagni, M., Xhaferraj, L., 2021. Raw material prices increase. DOI: 10.13140/RG.2.2.10320.43526.

Brinson, L.C., 1993. One-Dimensional Constitutive Behavior of Shape Memory Alloys: Thermomechanical Derivation with Non-Constant Material Functions and Redefined

Martensite Internal Variable. J. Intel. Mat. Syst. Srt. 4 (2), 229–242. https://doi.org/10.1177/1045389X9300400213.

Cao, J., Xiong, H., Liu, Y., Yu, D., Chen, J., 2022. Seismic performance of glulam timber post and beam structures with and without light frame timber shear wall infill. J. Build. Eng. 57, 104965.

de Castro Motta, J., Qaderi, S., Farina, I. Singh, N., Amendola, A., Fraternali, F., 2022. Experimental characterization and mechanical modeling of additively manufactured TPU components of innovative seismic isolators. Acta Mech., Online First, DOI: 10.1007/s00707-022-03447-5.

Chang, B.C., Shaw, J.A., Iadicola, M.A., 2006. Thermodynamics of shape memory alloy wire: modeling, experiments, and application. Contin. Mech. Thermodyn. 18, 83–118. https://doi.org/10.1007/s00161-006-0022-9.

dell'Isola, F., Seppecher, P., Alibert, J.J., Lekszycki, T., Grygoruk, R., Pawlikowski, M., Steigmann, D., Giorgio, I., Andreaus, U., Turco, E., Gołaszewski, M., Rizzi, N., Boutin, C., Eremeyev, V.A., Misra, A., Placidi, L., Barchiesi, E., Greco, L., Cuomo, M., Cazzani, A., Corte, A.D., Battista, A., Scerrato, D., Eremeeva, I.Z., Rahali, Y., Ganghoffer, J.-F., Müller, W., Ganzosch, G., Spagnuolo, M., Pfaff, A., Barcz, K., Hoschke, K., Neggers, J., Hild, F., 2019. Pantographic metamaterials: an example of mathematically driven design and of its technological challenges. Continuum Mech. Thermodyn. 31 (4), 851–884.

Dong, W., Li, M., Lee, C.L., MacRae, G., Abu, A., 2020. Experimental testing of full-scale glulam frames with buckling restrained braces. Eng. Struct. 222, 111081 https://doi.org/10.1016/j.engstruct.2020.111081.

Dunne, C.F., Roche, K., Twomey, B., Hodgson, D., Stanton, K.T., 2015. Blast coating of superelastic NiTi wire with PTFE to enhance wear properties. Shape Mem. Superelasticity 1 (1), 41–49. https://doi.org/10.1007/s40830-015-0004-5.

Fraternali, F., De Chiara, E., Skelton, R., 2015. On the use of tensegrity structures for kinetic solar façades of smart buildings. Smart Mater. Struct. 24 (10) https://doi.org/10.1088/0964-1726/24/10/105032.

Fraternali, F., Santos, F., 2019. Mechanical modeling of superelastic tensegrity braces for earthquake-proof structures. Extreme Mech. Lett. 33, 100578 https://doi.org/10.1016/j.eml.2019.100578.

Fraternali, F., Singh, N., Amendola, A., Benzoni, G., Milton, G.W., 2021. A biomimetic sliding–stretching approach to seismic isolation. Nonlinear Dyn. 106 (4), 3147–3159.

Graesser, E.J., Cozzarelli, A., 1991. Shape-memory alloys as new materials for aseismic isolation. J. Eng. Mech. 117, 2590–26084. https://doi.org/10.1061/(ASCE)0733-9399(1991)117:11(2590).

Hmede, H., Chapelle, F., Lapusta, Y., 2022. Review of neural network modeling of shape memory alloys. Sensors 22 (15), 5610. https://doi.org/10.3390/s22155610.

Hu, S., Qiu, C., Zhu, S., 2022. Machine learning-driven performance-based seismic design of hybrid self-centering braced frames with SMA braces and viscous dampers. Smart Mater. Struct. 31 (10), 105024 https://doi.org/10.1088/1361-665X/ac8efc.

International Renewable Energy Agency (IRENA) A. Dhabi. www.irena.org. Global energy transformation: A roadmap to 2050, International Renewable Energy Agency 2021.

IPCC, 2021. Summary for policymakers. In: Climate Change, 2021: The physical science cases. Contribution of working group I to the sixth assessment report of the intergovernmental panel on climate change [Masson-Delmotte, V. et al. (eds.)]. Cambridge University Press.

Li, C., Zhou, Z., Zhu, Y., 2019. A uniaxial constitutive model for NiTi shape memory alloy bars considering the effect of residual strain. J. Intell. Mater. Syst. Struct. 30 (8), 1163–1177. https://doi.org/10.1177/1045389X19835932.

Liu, M., Zhou, P., Li, H., 2018. Novel self-centering negative stiffness damper based on combination of shape memory alloy and prepressed springs. J. Aerosp. Eng. 31 (6), 04018100. https://doi.org/10.1061/(ASCE)AS.1943-5525.0000926.

Liu, Y., Zwingmann, B., Schlaich, M., 2015. Carbon fiber reinforced polymer for cable structures-a review. Polymers 7 (10), 2078–2099. https://doi.org/10.3390/polym7101501.

Luo, J., He, M., Li, Z., Ou, J., He, G., 2022. Seismic performance evaluation of glulam structures with either braced frames or knee-braced frames as the main lateral load resisting system. Soil Dyn. Earthq. Eng. 154, 107134 https://doi.org/10.1016/j.soildyn.2021.107134.

Menna, C., Auricchio, F., Asprone, D., 2015. Applications of shape memory alloys in structural engineering. In: Concilio, L., Lecce, A. (Eds.), Shape Memory Alloy Engineering. Butterworth-Heinemann, Boston, pp. 369–403. https://doi.org/10.1016/B978-0-08-099920-3.00013-9.

Nagase, K., Skelton, R.E., 2014. Minimal mass tensegrity structures. J. Int. Assoc. Shell Spat. Struct. 55 (1), 37–48.

Ozbulut, O.E., Hurlebaus, S., 2010. Neuro-fuzzy modeling of temperature-and strain-rate-dependent behavior of NiTi shape memory alloys for seismic applications. J. Intel. Mater. Syst. Struct. 21 (8), 837–849. https://doi.org/10.1177/1045389X10369720.

Polastri, A., Izzi, M., Pozza, L., Loss, C., Smith, I., 2019. Seismic analysis of multi-storey timber buildings braced with a CLT core and perimeter shear-walls. Bull. Earthq. Eng. 17 (2), 1009–1028. https://doi.org/10.1007/s10518-018-0467-9.

Pomponi, F., Hart, J., Arehart, J.H., D'Amico, B., 2020. Buildings as a global carbon sink? A reality check on feasibility limits. One Earth 3, 157–161. https://doi.org/10.1016/j.oneear.2020.07.018.

Ponzo, F.C., Di Cesare, A., Lamarucciola, N., Nigro, D., 2019. Seismic design and testing of post-tensioned timber buildings with dissipative bracing systems. Front. Built. Environ. 5, 104. https://doi.org/10.3389/fbuil.2019.00104.

Salvadori, V., 2021. Multi-storey timber-based buildings: An international survey of case-studies with five or more storeys over the last twenty years. PhD Thesis, Technischen Universität Wien, DOI: 10.13140/RG.2.2.14822.55360.

Sandhaas, C., Sarnaghi, A.K., van de Kuilen, J., 2020. Numerical modelling of timber and timber joints: Computational aspects. Wood Sci. Technol. 54 (1), 31–61. https://doi.org/10.1007/s00226-019-01142-8.

Santos, F., Benzoni, G., Fraternali, F., 2019. Seismic performance of superelastic tensegrity braces. Ingegneria Sismica – Int. J. Earthq. Eng. 36 (3), 20–37.

Santos, F., Caroço, C., Amendola, A., Miniaci, M., Fraternali, F., 2022. 3D tensegrity braces with superelastic response for seismic control. Int. J. Multiscale Comput. Eng. 20 (5), 53–64. https://doi.org/10.1615/IntJMultCompEng.2022041968.

Schuster, S., Geier, S., 2022. Towards circularity in timber construction in the German context. IOP Conf. Ser.: Earth Environ. Sci. 1078, 012030. https://doi.org/10.1088/1755-1315/1078/1/012030.

Skelton, R.E., de Oliveira, M.C., 2010. Tensegrity Systems. Springer.

Svatoš-Ražnjević, H., Orozco, L., Menges, A., 2022. Advanced timber construction industry: A review of 350 multi-storey timber projects from 2000–2021. Buildings 12 (4), 404. https://doi.org/10.3390/buildings12040404.

United Nations Environment Programme, 2021. Global status report for buildings and construction: towards a zero-emission, efficient and resilient buildings and construction sector. Nairobi. www.globalabc.org (accessed 01/27/2023).

Wang, W., Fang, C., Liu, J., 2016. Large size superelastic SMA bars: Heat treatment strategy, mechanical property and seismic application. Smart Mater. Struct. 25 (7), 075001 https://doi.org/10.1088/0964-1726/25/7/075001.

Wang, Z., Luo, J., Kuang, W., Jin, M., Liu, G., Jin, X., Shen, Y., 2022. Strain rate effect on the thermomechanical behavior of NiTi shape memory alloys: A literature review. Metals 13 (1), 58. https://doi.org/10.3390/met13010058.

Wang, B., Zhu, S., 2018. Cyclic tension–compression behavior of superelastic shape memory alloy bars with buckling-restrained devices. Constr. Build. Mater. 186, 103–113. https://doi.org/10.1016/j.conbuildmat.2018.07.047.

Yeom, H.-J., Yoo, J.-H., 2018. Analytical investigation on seismic behavior of inverted V-braced frames. Int. J. Steel Struct. 18 (1), 189–198. https://doi.org/10.1007/s13296-018-0315-4.

Zhou, P., Liu, M., Li, H., Song, G.B., 2018. Experimental investigations on seismic control of cable-stayed bridges using shape memory alloy self-centering dampers. Struct. Control Health Monit. 25 (7), e2180.